MATERIALS DESIGN

A stoichiometrically conserved homologous series with infinite structural diversity

Hengdi Zhao[1], Xiuquan Zhou[1,2], Ziliang Wang[3], Patricia E. Meza[3], Yihao Wang[1], Denis T. Keane[4], Steven J. Weigand[4], Saul H. Lapidus[5], Duck-Young Chung[1], Christopher Wolverton[3], Vinayak P. Dravid[3], Stephan Rosenkranz[1], Mercouri G. Kanatzidis[1,6]*

We describe a compositionally guided structural evolution within a stoichiometrically conserved framework, $BaSbQ_3$ ($Q = Te_{1-x}S_x$), where each value of x gives rise to a distinct phase. The fundamental building blocks, A_1 ($BaSbSTe_2$) and B_n ($Ba_nSb_nS_{n-1}Te_{2n+1}$), were composed of modular double rocksalt slabs stacked with functional polytelluride zigzag chains, with each phase differing only in the size and assembly of these blocks. Ten compounds were synthesized that maintained a coherent chemical identity that arose from this isovalent, isoelectronic substitution of Te and S. We envision that the phase formation at a molecular level unfolds in stages of extension, termination, and assembly and propose a design concept of "anionic disparity," where phase homologies and polytelluride hierarchical networks can be controlled by leveraging differences in anion electron affinity and sizes.

A central ambition in materials science is the predictive synthesis of compounds with targeted structures and functions. Molecular systems have seen notable design control, but achieving similar precision in extended inorganic frameworks remains elusive, as small compositional changes can trigger abrupt structural shifts. This difficulty arises not from lack of synthetic skill, but from incomplete understanding of the structure-directing principles that govern crystallization. Homologous series offer an underutilized opportunity to uncover principles linking composition and structure for achieving structural predictability and compositional control.

Phase homologies in inorganic chemistry trace back to the foundational work of Magnéli and collaborators, who, in the 1950s, reported a systematic series of nonstoichiometric titanium oxides (Ti_nO_{2n-1}) formed through crystallographic shear mechanisms, where each member has a different stoichiometry (*1*). These Magnéli phases revealed that complex solids could be organized into homologous families with predictable structural motifs and stoichiometries (*1*, *2*). This concept was further extended to oxides (*3*–*5*), intermetallics (*6*–*10*), chalcogenides (*11*–*14*), and halides (*15*, *16*) in subsequent decades, offering a pathway toward rationalizing and discovering new compounds.

Although considerable progress has recently been claimed in using machine learning (ML) and artificial intelligence (AI) (*17*–*19*) to predict vast numbers of hypothetical materials, their effectiveness has been criticized recently (*20*, *21*). Constrained primarily by substituting elements within known structures, their predictive power is largely limited to materials with established structure types, leaving those with truly new structures or metastable phases beyond reach. Therefore, predicting chemically sound and experimentally synthesizable phases with new structures remains a challenge for extended solids.

By contrast, the search for new compounds with AI and ML has been notably more successful in fields where more extensive sets of chemical principles have been established, such as organic (*22*–*26*) and molecular (*27*, *28*) chemistry. To bridge this design-rules gap in solid-state chemistry, it is essential to develop powerful chemically intuitive frameworks, such as phase homologies, that provide both predictive structure-composition relationships and practical guidance for synthesis. Our group has emphasized the predictive power of phase homologies as "compound-generating machines," using them not only to classify known solids but also to guide the deterministic design and synthesis of entirely new materials with defined structural architectures (*11*, *12*).

Here, we introduce a design concept, termed "anionic disparity," to create and control structural homologies through targeted anion mixing. This principle leverages the differential electron affinities of anionic species to both direct their site occupancy, forming new ordered multianion structures, and concurrently manipulate the electron distribution within anionic substructures. Specifically, we applied this concept to the starting compound $BaSbTe_3$, which features alternating double rocksalt slabs and polytelluride zigzag chains, to address the challenge of controlling tellurium-based structure motifs.

We present the chemical rules that generate the homologous members and how these rules can be used to design new members. We initially hypothesized that starting from $BaSbTe_3$, the isoelectronic substitution of sulfur for isovalent tellurium could lead to one of three outcomes: (i) a solid solution with random S and Te (S/Te) substitution; (ii) an ordered multianion arrangement of S and Te within the $BaSbTe_3$ structure (*29*); or (iii) a frustrated scenario in which the disparity in bonding drives a complete destabilization of the original structure, giving rise to a new framework. However, the outcome was not any of the expected scenarios. Instead, we observed the emergence of a previously unknown class of structurally related compounds, a polymorphic homologous series, where all members shared the same nominal composition $BaSbQ_3$ ($Q = Te_{1-x}S_x$) yet exhibited distinct and systematically evolving structures. We outline design rules and then describe each member of this series in detail and sequence, starting with the Te-rich end member and proceeding through phases with progressively higher sulfur content.

Design principles

We hypothesized that by introducing a more electronegative but isovalent element from the same group of the periodic table, such as sulfur, into a chemical system containing different types of telluride anions, such as Te^{2-} and polytelluride $[Te_n]^{2-}$ anions, we could avoid formation of solid solutions by taking advantage of the large difference in size and electronegativity and instead induce a preferential ordering between the two types of chalcogenide ions. We further hypothesized that the constant sum of cationic contributions from Ba and Sb would disproportionately amplify the anionic disparity between sulfur and tellurium.

Sulfur, with its higher electron affinity, selectively occupies the more electron-rich Te^{2-} sites, forming a new ordered multianion structure. This selective substitution of Te^{2-} with S^{2-} also effectively modifies electron distributions within the tellurium network, transforming more remaining tellurium from electron-rich telluride Te^{2-} to the more electron-poor polytelluride state of $[Te_n]^{2-}$. These reactions would drive the structural evolution of different polytelluride hierarchical networks from single zigzag chains to extended square nets. This hypothesis is consistent with the observations that S substitutions systematically promote an enriched polytelluride fraction (Table 1). This strategy was deemed possible because single polytelluride zigzag chains and extended polytelluride square nets have been observed in $BaSbTe_3$ (*30*) and $BaSbSTe_2$ (*31*), respectively.

[1]Materials Science Division, Argonne National Laboratory, Lemont, IL, USA. [2]Department of Chemistry, Georgetown University, Washington, DC, USA. [3]Department of Materials Science and Engineering, Northwestern University, Evanston, IL, USA. [4]DuPont-Northwestern-Dow Collaborative Access Team (DND-CAT) Synchrotron Research Center, Northwestern University, Lemont, IL, USA. [5]X-ray Science Division, Advanced Photon Source, Argonne National Laboratory, Argonne, IL, USA. [6]Department of Chemistry, Northwestern University, Evanston, IL, USA. *Corresponding author. Email: m-kanatzidis@northwestern.edu

Table 1. Summary of crystal structures of synthesized homologous phases from single-crystal x-ray diffraction at 293 K. Note that all chemical formulas are normalized to $Z = 2$ for comparison, where Z is the number of formula units per unit cell. [Te_n] represents polytelluride, and Te refers to all tellurium contents. Detailed coordination and bond-distance analyses can be found in the supplementary materials.

Phase	Homologous value	Formula	Space group	Structure type	Ribbon [Te_n]	S/Te ratio	[Te_n]/Te ratio
I	$(B_2)_2$	$Ba_4Sb_4Te_{12}$	$P2_12_12_1$	$BaBiSe_3$	$[Te_2]^{2-}$	0	0.17
II	$(B_4)_2$	$Ba_8Sb_8S_6Te_{18}$	$P2_12_12_1$	$SrBiSe_3$	$[Te_3]^{2-}$	0.33	0.33
III	A_1B_4	$Ba_5Sb_5S_4Te_{11}$	$P2_1/m$	New	$[Te_3]^{1-}$	0.36	0.27
IV	A_1B_5	$Ba_6Sb_6S_5Te_{13}$	$P2_1/m$	New	$[Te_4]^{2-}$	0.38	0.31
V	A_1B_6	$Ba_7Sb_7S_6Te_{15}$	$P2_1/m$	New	$[Te_5]^{3-}$	0.4	0.33
VI	A_1B_7	$Ba_8Sb_8S_7Te_{17}$	$P2_1/m$	New	$[Te_6]^{4-}$	0.41	0.35
VII	B_4B_5	$Ba_9Sb_9S_7Te_{20}$	$P2_1/m$	New	$[Te_7]^{5-}$	0.35	0.35
VIII	$A_1B_4(B_5)_2$	$Ba_{15}Sb_{15}S_{12}Te_{33}$	$P2_1/m$	New	$[Te_{11}]^{7-}$	0.36	0.33
IX	$(A_1)_2(B_5)_4$	$Ba_{22}Sb_{22}S_{18}Te_{48}$	*Pnma*	New	$[Te_{16}]^{10-}$	0.38	0.33
X	B_∞	$BaSbSTe_2$	*Pmm2*(0β0)000	$SrBiTe_3$	$[Te]^{1-}$	0.5	0.5

Guided by this design principle, we synthesized 10 representative members of a new homologous series of $BaSbQ_3$ (Q = $Te_{1-x}S_x$) (Table 1). Each compound exhibits a distinct crystal structure type, yet all members share the same nominal composition of Ba:Sb:Q equal to 1:1:3, and the progression in structure from one member to the next was predictable. All structures in this homology comprise two types of fundamental building blocks. One is a two-octahedra-wide rocksalt slab, noted as A_1 = $BaSbSTe_2$, and the other is a modular rocksalt slab stacked with adjustable polytelluride chains, formulated as $B_n = Ba_nSb_nS_{n-1}Te_{2n+1}$ or $B_n = Ba_nSb_nS_{n-1}Te_{n+2}[Te_{n-1}]$, with [$Te_n$] representing the polytelluride component. The polytelluride component scaled with the S/Te-substitution levels (Table 1), reaffirming the anion-driven structural evolutions.

The difference from one member to the next was primarily the length of the modular blocks and the connectivity of all blocks, which is governed by the S/Te ratio. In this homologous family of $BaSbQ_3$, the anion disparity between Te and S offered an effective method to control the size of the polytelluride networks. The increasing S fraction in the formula $BaSbQ_3$ systematically reconfigured the polytelluride fragments in the structure and led to a continuous evolution from a single zigzag polytelluride chain to infinitely extended two-dimensional polytelluride square nets.

Homologous phase evolution of A_mB_n = $(BaSbSTe_2)_m(Ba_nSb_nS_{n-1}Te_{2n+1})$

Phase I (Fig. 1A; $BaSbTe_3$, or $Ba_4Sb_4Te_{10}[Te_2]$, where [Te] specifies the polytelluride) represents the Te-only, first member of the homologous series without sulfur incorporation. It crystallized in the $BaBiSe_3$-type structure (*30*, *32*) in the orthorhombic space group $P2_12_12_1$ (space group no. 19) with a = 4.6240(9) Å, b = 16.915(3) Å, and c = 18.058(4) Å (numbers in parentheses are errors in the last digit). A two-block-wide distorted double rocksalt slab of (Sb_4Te_{10}) alternates with one polytelluride zigzag chain of [Te_2] along the b axis, with Ba cations sandwiched in between (Fig. 1A). Each ($Ba_4Sb_4Te_{10}$)[Te_2] block is mirror reflected along the b axis and connects between the ($Ba_4Sb_4Te_{10}$) double rocksalt slab and the [Te_2] zigzag Te chain of its adjacent neighbor along the c axis, forming a larger orthorhombic cell with the space group of $P2_12_12_1$. Both the double rocksalt slabs and the zigzag chains extend infinitely along the a axis, forming the infinite slabs and chains (fig. S1B).

With the substitutional incorporation of a small amount of sulfur, we observed **Phase II** (Fig. 1C; $Ba_8Sb_8S_6Te_{18}$ or $Ba_8Sb_8S_6Te_{12}[Te_6]$), isostructural with $SrBiSe_3$ (*33*), also crystallized in the orthorhombic space group $P2_12_12_1$ (no. 19) with a = 4.4476(4) Å, b = 16.5502(14) Å, and c = 35.400(3) Å. Similar to **Phase I**, it also featured alternating double rocksalt slabs and polytelluride zigzag chains separated by Ba cations. However, both double rocksalt slabs and polytelluride chains were widened to be a four-block-wide double rocksalt slab of ($Ba_8Sb_8S_6Te_{12}$) stacked with three polytelluride zigzag chains of [Te_6]. The fact that this small level of S substitution results in an entire phase homology rather than a simple solid solution of **Phase I** (scenario 1) or an ordered substitution within the parent lattice (scenario 2) suggests a far more intricate formation mechanism.

By incorporating more sulfur into our synthesis, we obtained **Phase III** (Fig. 1J; $Ba_5Sb_5S_4Te_{11}$, or $Ba_5Sb_5S_4Te_8[Te_3]$), which crystallized in a new structure type in the monoclinic space group $P2_1/m$ (no. 11) with a = 16.630(3) Å, b = 4.4864(9) Å, c = 22.494(5) Å, and β = 99.63(3)°. Similar to **Phase II**, it also hosted the four-block-wide double rocksalt slabs of ($Sb_8S_6Te_{12}$) alternating with three-polytelluride zigzag chains of [Te_6] along the a axis, with Ba cations interspersed. Differently, each ($Ba_8Sb_8S_6Te_{12}$)[Te_6] block in **Phase III** is parallel to its neighbor and bridged by another isolated one-block-wide double rocksalt slab of ($Sb_2S_2Te_4$) surrounded by Ba^{2+} cations. This bridging unit (highlighted in light blue in Fig. 1J) is a key feature distinguishing **Phase III** from **Phase II**.

As noted above, these phases can be described in terms of the A_1 block (light blue fragment in Fig. 1P) and the B_n ($n \geq 2$) blocks (darker blue; a representative B_4 fragment is shown in Fig. 1P). Each B_n fragment consists of two capping, or "*C*" fragments (gray-shaded blocks), with (n−2) extendable "*E*" fragments (navy blue–shaded blocks) inserted in between (in general, each B_n can be expressed as $E_{n-2}C_2$). Note that the *E* and *C* fragments differ both structurally and compositionally in anions. Using this notation, **Phases I**, **II**, and **III** can be expressed as $(B_2)_2$, $(B_4)_2$, and A_1B_4, respectively. Intriguingly, the B_n block can be further extended, which leads to the formation of **Phase IV** (Fig. 1K; $Ba_6Sb_6S_5Te_{13}$, A_1B_5), **Phase V** (Fig. 1L; $Ba_7Sb_7S_6Te_{15}$, A_1B_6), **Phase VI** (Fig. 1M; $Ba_7Sb_8S_7Te_{17}$, A_1B_7), and, lastly, **Phase X** [Fig. 1O; $BaSbSTe_2$, B_∞ (*31*)], with incremental length of B_n fragments between each phase. These phases demonstrate that A_1 and B_n fragments can act as robust modular fundamental building blocks for rational structural assembly. Leveraging the predictive framework of phase homologies, we propose that additional hypothetical structures, indicated by dashed, semi-transparent boxes in Fig. 1, fill the gaps between the known phases.

The above seven phases shown in Fig. 1 are homologs and can be generalized with the chemical formula of $A_mB_n = (BaSbSTe_2)_m$ ($Ba_nSb_nS_{n-1}Te_{2n+1}$), or $A_mB_n = (BaSbSTe_2)_m(Ba_nSb_nS_{n-1}Te_{n+2}[Te_{n-1}])$, where $m = [0, 1]$ and $n \geq 2$. This notation describes a series of specific phases starting from **Phase I**, with two modular blocks featuring rocksalt slabs and polytellurides, A_m and B_n (Fig. 1). The n values signify the length of the B_n blocks. When $m = 0$, the phases lack the A_m block, as shown in the left column of Fig. 1. The right column displays members that contain both A_m and B_n blocks. The B_n backbone extends by the

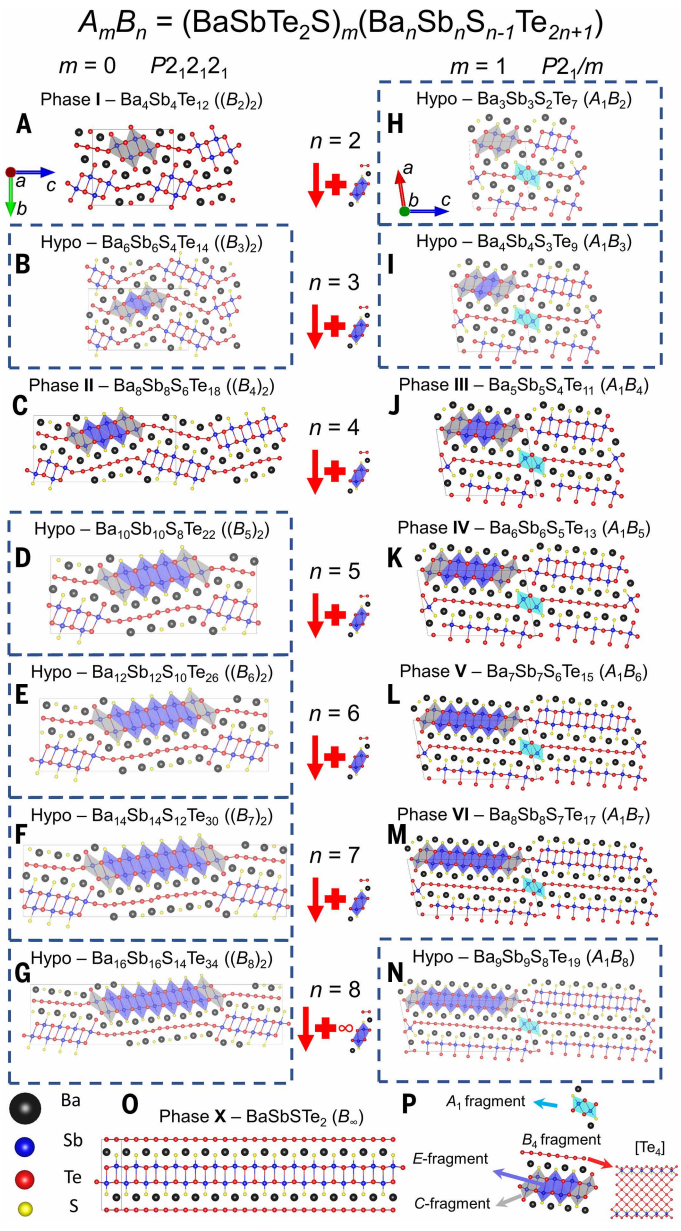

Fig. 1. Crystal structures. Both known and hypothetical structures are shown for the $m = 0$ and $m = 1$ series. The hypothetical structures (hypo) are faded and marked by a dashed box, with adjusted transparency. (**A** to **G**) $(B_n)_2$, and (**H** to **N**) A_1B_n phases, with $n = [2, 8]$, and (**O**) the B_∞ phase. The evolution of the modular B_n building block that essentially differentiated each adjacent phase is shown in the middle column. (**P**) The individual A_1 fragment (marked by light blue color) and a representative B_4 fragment with highlighted extendable *E* rocksalt part (navy blue color), capping rocksalt part *C* (gray color), and the polytelluride of [Te_4].

addition of (E_1, or BaSbSTe[Te]) units, which increases the length of both the rocksalt slabs and the associated polytelluride ribbons. Furthermore, by collectively depicting both S and Te as chalcogen (Q), the general chemical formula can be rewritten as $A_mB_n = [BaSbQ_3]_{m+n}$.

Energetic proximity and hierarchical assembly of homologous phases

First-principles calculations of these homologous series revealed both metastability and proximity in the formation energies among all 10 experimentally discovered phases (table S1). Typical density functional theory (DFT) formation energies can have inherent uncertainties, even with corrections, that may span tens of milli–electron volts per atom (*34*). However, our calculated energy differences among these phases, excluding the end members (**Phases I** and **X**), fall well within such margins (~10 meV; table S1). The energetic proximity among these essentially degenerate polymorphs suggests that their selective formation was not driven by simple thermodynamic stabilization. Furthermore, the stepwise addition of B_n that formed multiple polymorphs, analogous to the addition of CH_2 in alkenes, suggests an unconventional phase-formation mechanism. The structural evolution unfolds in three conceptual stages: extension, termination, and assembly.

Extension

The reaction starts with many extendable fragments of $Sb_2S_2Te_2$ (E_1 fragments, marked in Fig. 2B) dissolved inside the reaction container (Fig. 2A). When two E_1 fragments bond between Sb and Te, a two-block-wide E_2 fragment is formed (Fig. 2C). Subsequently, the two-block-wide E_2 fragments can add another E_1, forming a three-block-wide E_3 fragment (Fig. 2D). This chain addition process systematically expands the rocksalt-like backbone.

Termination

The extension process terminates when a C_1 fragment adds to each side of E_n and forms an E_nC_2 fragment (Fig. 2E). Termination occurs because the C_1 fragment exhibits a different degree of distortion than the E_1 fragment (see detailed discussion in the supplementary materials and figs. S11 to S14). As the length of the E_n fragment increases, accumulated distortions lead to steric frustration in packing S and Te atoms efficiently, making the addition of another E_1 fragment energetically or sterically unfavorable. The C_1 fragment effectively satisfies the reactive edge of the growing E_n fragment in a manner that another E_1 unit cannot, thereby halting the one-dimensional extension of the rocksalt slab. This step is analogous to chain-termination reactions in polymerization processes.

Assembly

Both the $E_{n-2}C_2$ and [Te_n] polytelluride chains are negatively charged and stabilized with Ba^{2+} cations as the bridge, assembling as B_n (Fig. 2F). Similarly, the A_1 fragment is assembled from E_1 and one polytelluride chain (Fig. 2G). Finally, with a sufficiently high concentration of the required molecular fragments, they assemble into extended solids. For instance, with B_4 fragments as the only dominating fragments, **Phase II** [$(B_4)_2$] consists of alternating B_4 fragment forms (Fig. 2H). Conversely, with coexisting B_4 and A_1 fragments, the phase would shift to **Phase III** (A_1B_4), which is made of B_4 fragments bridged by A_1 blocks (Fig. 2I). After assembly, each A_1 and B_n block contributes as A_1 = BaSbSTe$_2$ and $B_n = Ba_nSb_nS_{n-1}Te_{n+2}[Te]_{n-1}$, respectively, with [$Te_n$] representing the polytelluride fragments.

In addition, the conceptual stages discussed above also suggest that the reaction vessel could host many different B_n fragments simultaneously (Fig. 2A), which is implied by the observation of additional phases such as **Phase VII** (Fig. 3, A and B; $Ba_9Sb_9S_7Te_{20}$, B_4B_5), **Phase VIII** [Fig. 3, C, D, and G; $Ba_{15}Sb_{15}S_{12}Te_{33}$, $A_1B_4(B_5)_2$], and **Phase IX** [Fig. 3, E and F; $Ba_{22}Sb_{22}S_{18}Te_{48}$, $(A_1)_2(B_5)_4$], where various B_n fragments coprecipitate into long-range ordered crystal structures. To be more specific, **Phase VII** (Fig. 3B; B_4B_5) consists of one B_4 block alternating with another B_5 block along the *c* axis (Fig. 3A), whereas **Phase VIII** [Fig. 3D; $A_1B_4(B_5)_2$] is built from one B_4 block, one B_5 block, and another B_5 block that couples with an A_1 block (Fig. 3, C and G). The alternating A_1-B_5-B_4-B_5 building blocks repeating along the *c* axis is also corroborated by the high-angle annular dark field image (Fig. 3G and figs. S28 and S29). Interestingly, this structure can also be viewed as the ordered intergrowth of one **Phase VII** (Fig. 3B; B_4B_5) connecting another **Phase IV** (Fig. 1K; A_1B_5) along the *c* axis. Finally, **Phase IX** [Fig. 3F; $(A_1)_2(B_5)_4$] is composed of two A_1 blocks

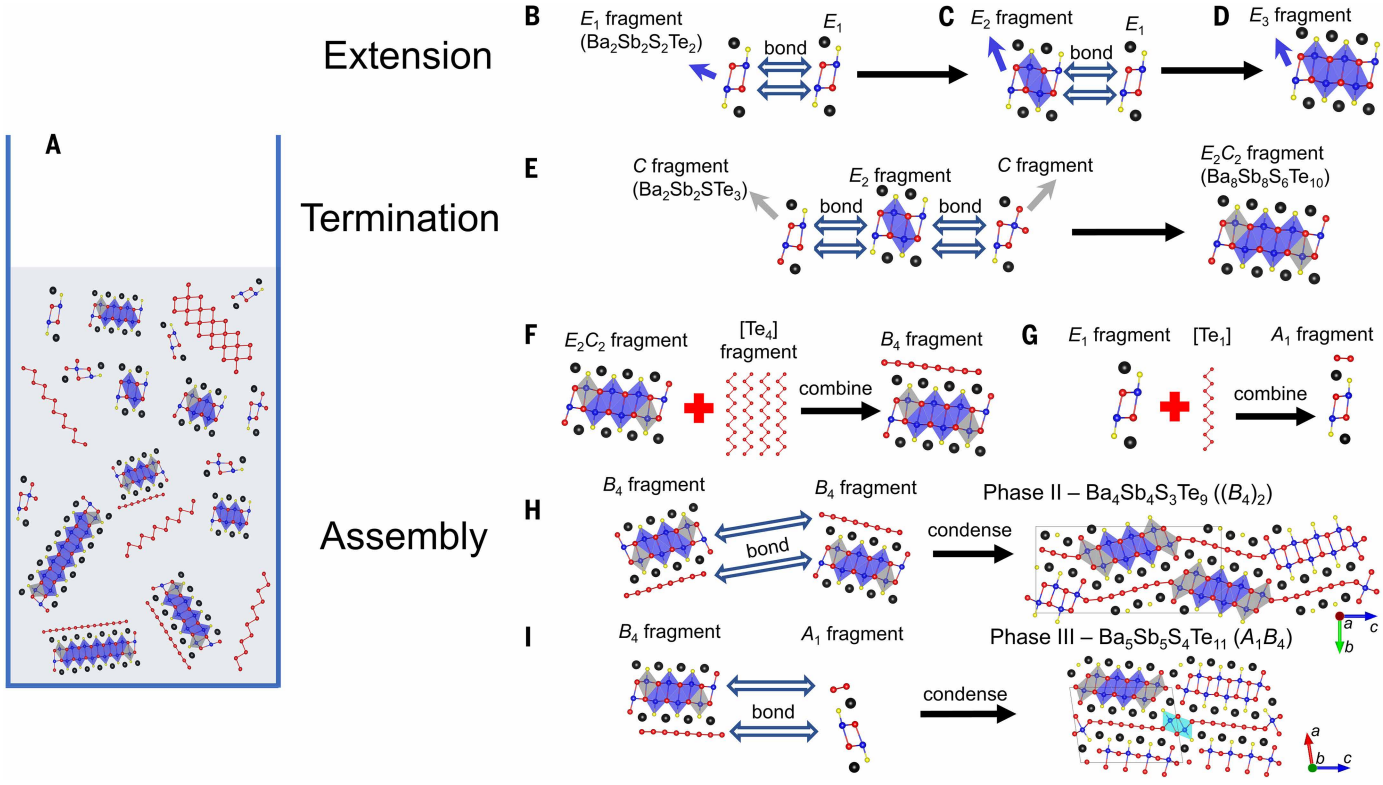

Fig. 2. A hypothetical phase-formation concept. (**A**) A schematic of the reaction vessel with different molecular fragments; the extension process from (**B**) E_1 to (**C**) E_2 and subsequently to (**D**) E_3, where E represents the extendable part of B_n fragments. (**E**) A representative termination process where a E_2 fragment is capped on each aside by the capping, C, assembling to an E_2C_2 molecular fragment. The representative assembly process of (**F**) an E_2C_2 fragment stacked with the polytelluride fragment, forming a B_4 fragment; (**G**) an E_1 fragment stacked with the polytelluride fragment, forming an A_1 fragment; (**H**) two B_4 fragments forming the $(B_4)_2$ phase; and (**I**) one A_1 fragment and another B_4 fragment forming the A_1B_4 phase.

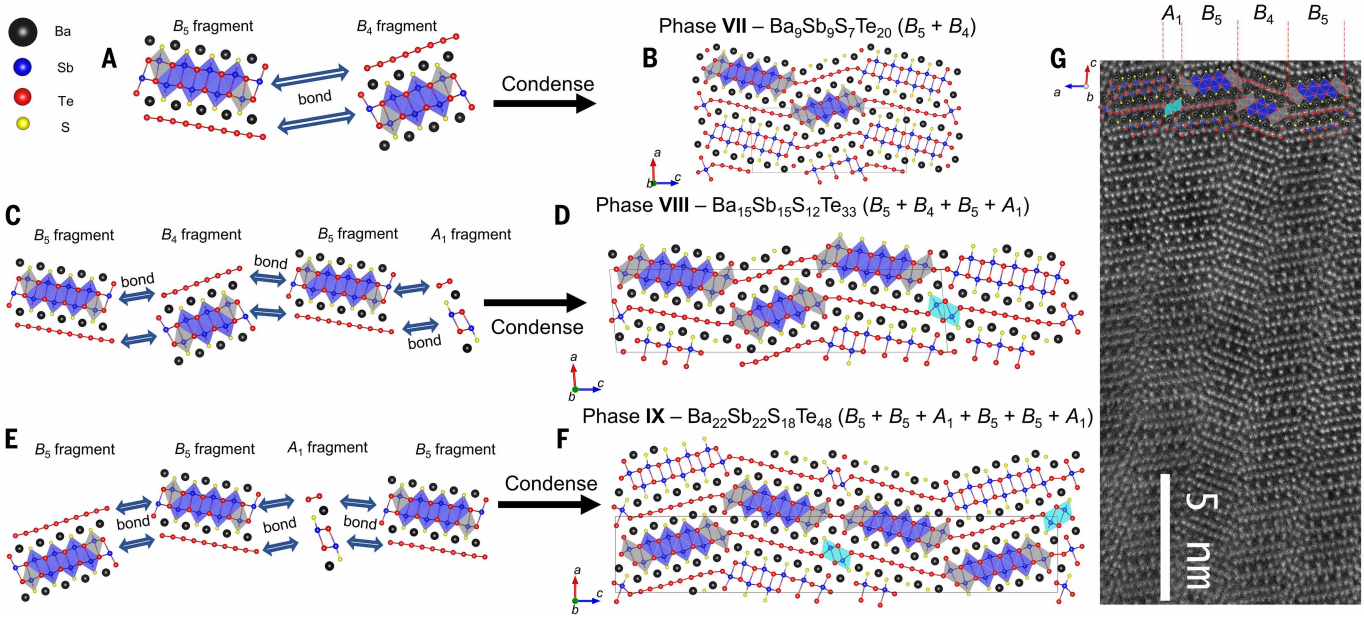

Fig. 3. Fragment assembly. The molecular fragments assembly process and crystal structure of (**A** and **B**) **Phase VII**, $Ba_9Sb_9S_7Te_{20}$, B_4B_5; (**C** and **D**) **Phase VIII**, $Ba_{15}Sb_{15}S_{12}Te_{33}$, $A_1B_4(B_5)_2$; and (**E** and **F**) **Phase IX**, $Ba_{22}Sb_{22}S_{18}Te_{48}$, $(A_1)_2(B_5)_4$. (**G**) The high-angle annular dark field image of **Phase VIII**, $Ba_{15}Sb_{15}S_{12}Te_{33}$, $A_1B_4(B_5)_2$, overlapped with the solved crystal structure model. Note that these phases incorporate multiple types of B_n fragments, highlighting the potential for modular assembly of diverse structures through flexible combinations of A_1 and B_n blocks.

and four B_5 blocks, whose structure can be viewed as sequentially connected B_5-B_5-A_1-B_5-B_5-A_1 fragments (Fig. 3E).

The potential of a nearly free combination of any number and length of different A_1 and B_n fragments, as demonstrated by **Phases VII** to **IX**, serves as further evidence for the existence of A_1 and B_n as fundamental building blocks, which form in situ first and assemble into extended solids. Another notable feature of this homologous family is the emergence of isomerism. The chemical formula of **Phase VIII** [Fig. 3D; $A_1B_4(B_5)_2$] can be reduced from $Ba_{15}Sb_{15}S_{12}Te_{33}$ to $(Ba_5Sb_5S_4Te_{11})_3$, which is identical to that of **Phase III** (Fig. 1J; $Ba_5Sb_5S_4Te_{11}$, A_1B_4). Thus, **Phases VIII** and **III** represent nearly energetically degenerate polymorphs, or constitutional isomers, based on the different connectivity and arrangement of A_1 and B_n building blocks, yielding the same overall stoichiometry but distinct crystal structures. The existence of such isomers points to a rich structural landscape that is accessible through the combinatorial assembly of the fundamental A_1 and B_n fragments.

Prediction of new homologous members

To accommodate any arbitrary combinations of different A_1 and B_n blocks, $\Sigma_{m,n}A_mB_n$, three indices are sufficient to describe the entire homologous series: the M index, which is the total number of A_1 blocks; the N index, which is the sum of n for all B_n blocks; and the L index, which is the number of B_n blocks involved. Structurally, the N and L indices separate the extendable (E_1) and the capping (C_1) parts of the B_n fragment, as they differ both structurally and compositionally.

Excluding **Phase I** as the only Te-only phase, any phase with the index of (M, N, L) can be described by the general formula of $Ba_{M+N}Sb_{M+N}S_{M+N-L}Te_{2M+2N+L}$ (or $Ba_{M+N}Sb_{M+N}S_{M+N-L}Te_{2M+N+2L}[Te_{N-L}]$), with ($N$−$L$) indicating the number of polytellurides. Note that the general formula can also be written as $(BaSbQ_3)_{M+N}$, forming the homologous series that all can be reduced to simply $BaSbQ_3$ (Q = S or Te). A detailed explanation regarding this general formula can be found in the supplementary materials.

The modular structure leads to predictable unit-cell parameters. Accordingly, all structures have unit-cell parameters with one short axis ~4.5 Å (b axis), another axis ~16.5 Å (a axis), and a third modular axis scaling with the index of (M, N, L). Ignoring the β angle differences, each A_1 block and E and C fragments in Fig. 1P scale roughly as 4.75, 4.338, and 4.52 Å, respectively. The comparison between the calculated and measured c axis is summarized in table S2. This simple model essentially captures the incremental features of the c axis well but, undesirably, overlooks the β angle information, which arises from the spatial orientations of building blocks.

To incorporate this missing piece of information, we adopted a more sophisticated calculation model that considers both the length and orientations of each building block. As evident from **Phases I** and **II** under the orthorhombic cell, each B_n fragment extends along the c axis and tilts along the a axis (Fig. 1, A and C), which can be described by a modular unit-cell matrix (see details in the supplementary materials). In addition, building blocks assemble into extended solids with staggered arrangements, that is, the first one tilts toward the ($+a$) direction, whereas the next one tilts toward the ($-a$) direction (fig. S20). Consequently, all $(B_n)_2$ phases crystallized with an orthorhombic cell as the tilting angle cancel out because of the staggered arrangements.

However, the mismatched sizes of the A_1 and B_n fragments lead to the monoclinic cells observed for each A_1B_n phase (Fig. 1, J to M), with β angles determined by the residual tilting angles due to incomplete cancellation. Furthermore, this prediction rule is not limited to $(B_n)_2$ and A_1B_n phases but extends to all homologous members, including those that involve more than one type of B_n block. For example, the slight β angle offset in **Phase VII** (Fig. 3B; B_4B_5) is a result of an incomplete cancellation of tilting angles caused by the different modular lengths of B_4 and B_5 fragments (Fig. 3A). By contrast, the orthorhombic structure of **Phase IX** [Fig. 3F; $(A_1)_2(B_5)_4$], whose structure features sequentially connected B_5-B_5-A_1-B_5-B_5-A_1 fragments (Fig. 3E), represents a case of completely compensated tilting angles.

A comparison of calculated and experimentally measured β angles and c axes that shows the promising predictive power of the unit-cell matrix method is summarized in table S3. The above calculation method also suggests that different arrangements from the same collection of molecular fragments would lead to slightly different unit-cell parameters, providing a method to distinguish such isomers. For instance, **Phase VIII** (B_5-B_4-B_5-A_1 connectivity) could have a hypothetical isomer with the B_5-B_5-B_4-A_1 connectivity under slightly different unit-cell parameters. A detailed discussion regarding how to use this calculation model to predict the unit-cell parameters can be found in the supplementary materials.

With the chemical composition and unit-cell parameters, the next essential information is the detailed atomic arrangements, which concern the connectivity between each molecular fragment and the space group symmetry. Based on all the synthesized structures, the involvement of the A_1 fragment or mismatched B_n fragments prefers centrosymmetric symmetry, with $Pnma$ and $P2_1/m$ for orthorhombic and monoclinic systems, respectively, whereas all phases with matched B_n fragments, such as $(B_n)_2$ phases, crystallize under the chiral $P2_12_12_1$ space group.

All structures can be viewed as sequentially connected fragments in a staggered way along the modular c axis. A mirror reflection along the ~16.5-Å crystal axis is performed on every other fragment, and all fragments assemble into extended solids, with the bond between the Sb from the SbQ_2 slab and the polytelluride [Te_n]. The above connectivity rule would likely limit the structure to containing only an even number of fragments, which is consistent with all 10 members that we observed (Table 1). Considering the simplest case of combining two types of fragments, connectivity with the same B_n results in $(B_n)_2$ phases (Fig. 1, A and C; **Phases I** and **II**), whereas the involvement of A_1 fragments leads to the formation of A_1B_n phases (Fig. 1, J to M; **Phases III** to **VI**).

Following these chemical principles, we successfully predicted multiple new homologous members belonging to $(B_n)_2$ and A_1B_n phases. Selected hypothetical structures are showcased in Fig. 1 to fill in the gaps between **Phases I** to **VI**, that is, Fig. 1, B and D to G, for $(B_n)_2$ phases and Fig. 1, H, I, and N, for A_1B_n phases. Encouragingly, although the $(B_3)_2$ phase in $BaSbQ_3$ is yet to be synthesized, its structure type has been observed (*35*, *36*), reaffirming the predictive power of the homologous method. Moreover, the summarized design rules can be naturally extended to accommodate any arbitrary number and length of A_1 and B_n fragments.

Polytelluride hierarchical networks controlled by electron affinity

The structural feature shared by the entire homologous family is the modular polytelluride fragments that continuously evolve from quasi–one-dimensional single zigzag chains, $(B_2)_2$, to quasi–two-dimensional square nets, B_∞. Telluride anions, $[Te_n]^{2-}$, compared with $[S_n]^{2-}$ and $[Se_n]^{2-}$, tend to have more versatile chain bondings (*37*). Because of its higher electron affinity and isovalent nature, S^{2-} preferentially substitutes the more electron-rich terminal Te^{2-} sites, which are on the outer side of each double rocksalt slab, leading to a rigid B_n fragment geometry shared by all homologous members. In these S/Te substitutions, the more electronegative S^{2-} ions selectively occupy rocksalt sites, whereas the polytelluride fragments remain composed exclusively of Te as $[Te_n]^{2-}$ units. In addition, the substitution of S also dedicates the systematic evolution of polytelluride hierarchical networks.

Such correlations are evident from the observations that the number of terminal sulfur sites scales with the number of polytelluride sites from the general formula of $B_n = Ba_nSb_nS_{n-1}Te_{n+2}[Te_{n-1}]$ (also in Fig. 4 and Table 1 with a correlated S/Te and [Te_n]/Te ratio). The valence state of polytelluride modulates with the length of B_n (Table 1), with

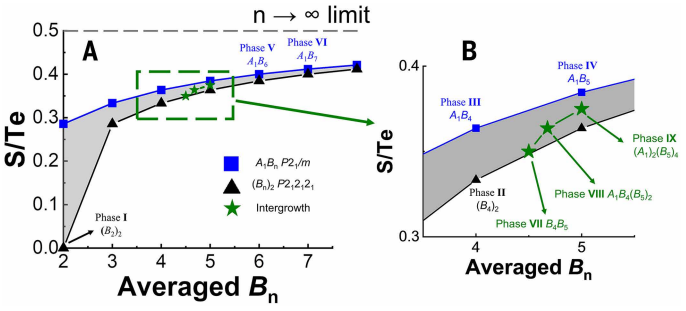

Fig. 4. Phase information. (**A**) Compositional phase diagram of the $BaSbQ_3$ (Q = S or Te) homologous series, organized by the S/Te ratio and the averaged B_n block length, with (**B**) an expanded view where interphase structures occur. Blue squares represent A_1B_n phases ($P2_1/m$), black triangles represent $(B_n)_2$ phases ($P2_12_12_1$), and green stars represent intergrowth phases composed of multiple building blocks, which can also be viewed as a linear combination of A_1B_n and $(B_n)_2$ phases. The gray-shaded region outlines the compositional range accessible to this homologous series. The smooth progression along this curve illustrates the systematic structural expansion enabled by anionic disparity and modular assembly.

the evolutions from $[Te_2]^{2-}$ dimers in **Phase I**, $(B_2)_2$, to $[Te_3]^{2-}$ trimers in **Phase II**, $(B_4)_2$, and eventually to square nets of Te with an incommensurately modulated charge density wave (CDW) in **Phase X**, B_∞ (*31*).

In addition, the inclusion of the A_1 block can fine-tune the electron distributions among polytelluride fragments, as each A_1 block carries a net –1 charge, expressed as $[BaSbSTe_2]^-$. Accordingly, the presence of A_1 fragments drives the polytelluride fragments to further buckle and maximize the Te···Te contacts in order to balance the charge, leading to an even more electron-poor configuration of polytelluride. As a result, the valence state of polytelluride for all A_1B_n phases scales as $[Te_n]^{(n-2)-}$ (Table 1). For instance, polytelluride networks forming nearly undistorted ribbons with Te···Te contact distances between 3.115 and 3.239 Å are observed in all A_1B_n phases (**Phases III** to **VI**; figs. S3 to S6), as compared to the dimers and trimers ($d_{Te\cdots Te}$ ~2.775 to 3.714 Å) in $(B_n)_2$ phases (**Phases I** and **II**; figs. S1 and S2).

As the polychalcogenide functional fragments are known to dictate physical properties, first-principles calculations reveal adjustable band gaps from 0.57 eV [fig. S24A; $(B_2)_2$] to 0.35 eV [fig. S24C; $(B_4)_2$] and eventually below the sensitivity of DFT calculations (fig. S24H; B_∞). The tunable electronic properties are also reflected in electrical transport measurements on selected homologous phases. As polytelluride networks continued to extend longer, diminishing electrical resistivity and activation gaps were observed (fig. S27). Note that the artificial metallicity of **Phase X** (fig. S24H; B_∞) with a strong Fermi surface-nesting effect is highly electronically unstable and can lead to emerging phenomena such as an incommensurate CDW order and pressure-induced superconductivity (*31*).

Figure 4 shows a compositional phase diagram of the discovered and predicted members according to their S/Te ratio and the average length of B_n building blocks. The structural boundaries between different homologous members and intergrowth phases highlight how structural complexity evolves with increasing sulfur content and B_n length. The smooth progression of phases along the plotted trend—marked by blue squares for A_1B_n compounds, black triangles for $(B_n)_2$ members, and green stars for intergrowth phases—illustrates how the systematic incorporation of sulfur leads to the modular expansion of structural motifs. The gray-shaded region delineates the compositional domain accessible within this homologous family and suggests where new members could be targeted. Figure 4 also highlights symmetry trends, with different structural types associated with distinct crystallographic space groups (e.g., $P2_1/m$ versus $P2_12_12_1$) and underscores the role of anionic disparity in driving the formation of increasingly complex architectures. Notably, the intergrowth phases demonstrate that the same overall composition can yield structurally distinct polymorphs through different arrangements of modular fragments, pointing to a form of unlimited structural isomerism, which is rare in inorganic solids.

Summary and outlook

We have unveiled a new homologous heterostructural series comprising at least 10 members with ordered multianion crystal structures with the same composition of $BaSbQ_3$ ($Q = Te_{1-x}S_x$), characterized by modular rocksalt slabs with adjustable functional polytelluride fragments. It is a family of stoichiomorphs, compounds of fixed stoichiometry but distinct structural identities driven by isovalent chalcogen mixing. The structural diversity is directly driven by systematic variation in composition, specifically the S/Te ratio. The formation and structural evolution of this series are driven by the difference in electron affinity between sulfur and tellurium under a constant cationic environment.

This chemical principle not only directs site-selective anion substitution but also dictates the fragmentation and condensation of polytelluride networks. The formation principle is based on extension, termination, and modular assembly at the molecular level. The structural coherence of these modular A_1 and B_n blocks is strongly supported by the discovery of ordered intergrowth phases (**Phases VII** to **IX**), where distinct motifs combine in a predictable and reproducible manner. Building on this insight, we have identified the underlying chemical rules that govern block compatibility and connectivity. These rules allow us to deterministically predict and design all yet-undiscovered A_1B_n and $(B_n)_2$ phases within this homologous family, establishing a framework that is readily adaptable to AI- and ML-guided materials discovery based on modular composition.

Despite the focus on anionic disparity in this work, the cation sites also present opportunities for further tuning and discovery. For instance, we have realized that previously reported seemingly unrelated compounds actually belong to this particular series. For example, $KThSb_2Se_6$ (*38*) and $BaLaBi_2Se_6$ (*38*) crystallize in the $(B_2)_2$ structure, and $KLa_2Sb_3S_9$ (*35*) and $TlLa_2Sb_3Se_9$ (*36*) in the $(B_3)_2$ structure, which suggests that further structural diversity with tunability is possible by focusing on the cation sites. All these materials are poised for exploration across a range of physical phenomena, including electronic, optical, and thermal transport behaviors.

REFERENCES AND NOTES

1. S. Andersson *et al.*, *Acta Chem. Scand.* **11**, 1641–1652 (1957).
2. A. Magnéli, *Acta Crystallogr.* **6**, 495–500 (1953).
3. S. Yudintsev, S. Stefanovskii, *Dokl. Earth Sci.* **401**, 319–325 (2005).
4. W. Gong *et al.*, *J. Am. Ceram. Soc.* **107**, 6574–6582 (2024).
5. B. Beznosikov, K. Aleksandrov, *Crystallogr. Rep.* **45**, 792–798 (2000).
6. J.-Y. Pivan, R. Guérin, M. Sergent, *J. Solid State Chem.* **68**, 11–21 (1987).
7. Y. M. Prots, W. Jeitschko, *Inorg. Chem.* **37**, 5431–5438 (1998).
8. L. Siggelkow, V. Hlukhyy, B. Wahl, T. F. Fässler, *Eur. J. Inorg. Chem.* **2011**, 4012–4024 (2011).
9. A. Weiland, J. B. Felder, G. T. McCandless, J. Y. Chan, *Chem. Mater.* **32**, 1575–1580 (2020).
10. A. Tursina, E. Khamitcaeva, A. Gribanov, D. Gnida, D. Kaczorowski, *Inorg. Chem.* **54**, 3439–3445 (2015).
11. A. Mrotzek, M. G. Kanatzidis, *Acc. Chem. Res.* **36**, 111–119 (2003).
12. M. G. Kanatzidis, *Acc. Chem. Res.* **38**, 359–368 (2005).
13. M. A. Viti, Z. Li, C. C. Laing, C. Wolverton, M. G. Kanatzidis, *J. Am. Chem. Soc.* **147**, 25350–25360 (2025).
14. M. A. Viti, Z. Li, C. Wolverton, M. G. Kanatzidis, *J. Am. Chem. Soc.* **147**, 29994–30008 (2025).
15. I. W. Gilley, T. E. Wiggins, E. H. Sargent, M. G. Kanatzidis, *Acc. Chem. Res.* **58**, 2243–2254 (2025).
16. E. S. Vasileiadou *et al.*, *J. Am. Chem. Soc.* **143**, 2523–2536 (2021).
17. A. Merchant *et al.*, *Nature* **624**, 80–85 (2023).
18. N. J. Szymanski *et al.*, *Nature* **624**, 86–91 (2023).
19. C. Zeni *et al.*, *Nature* **639**, 624–632 (2025).
20. J. Leeman *et al.*, *PRX Energy* **3**, 011002 (2024).

21. A. K. Cheetham, R. Seshadri, *Chem. Mater.* **36**, 3490–3495 (2024).
22. T. Dai *et al.*, *Nature* **635**, 890–897 (2024).
23. C. W. Coley *et al.*, *Science* **365**, eaax1566 (2019).
24. J. M. Granda, L. Donina, V. Dragone, D.-L. Long, L. Cronin, *Nature* **559**, 377–381 (2018).
25. A. F. de Almeida, R. Moreira, T. Rodrigues, *Nat. Rev. Chem.* **3**, 589–604 (2019).
26. M. H. S. Segler, M. Preuss, M. P. Waller, *Nature* **555**, 604–610 (2018).
27. K. T. Butler, D. W. Davies, H. Cartwright, O. Isayev, A. Walsh, *Nature* **559**, 547–555 (2018).
28. B. Sanchez-Lengeling, A. Aspuru-Guzik, *Science* **361**, 360–365 (2018).
29. A. Tassanov, H. Lee, Y. Xia, J. M. Hodges, *J. Am. Chem. Soc.* **146**, 32627–32639 (2024).
30. K. Volk, G. Cordier, R. Cook, H. Schäfer, *Z. Naturforsch. B. J. Chem. Sci.* **35**, 136–140 (1980).
31. Z.-Z. Luo *et al.*, *J. Am. Chem. Soc.* **147**, 6753–6762 (2025).
32. D.-Y. Chung *et al.*, *J. Am. Chem. Soc.* **119**, 2505–2515 (1997).
33. R. Cook, H. Schäfer, *Rev. chimie Minerale* **19**, 19–27 (1982).
34. J.-H. Pöhls, M. Heyberger, A. Mar, *J. Solid State Chem.* **290**, 121557 (2020).
35. S.-J. Kim, S.-J. Park, S.-A. Yim, *Bull. Korean Chem. Soc.* **25**, 485–490 (2004).
36. L. T. Menezes, Z. W. Richter-Bisson, A. Assoud, B. A. Kuropatwa, H. Kleinke, *Z. Anorg. Allg. Chem.* **647**, 81–85 (2021).
37. D. M. Smith, J. A. Ibers, *Coord. Chem. Rev.* **200–202**, 187–205 (2000).
38. K.-S. Choi, L. Iordanidis, K. Chondroudis, M. G. Kanatzidis, *Inorg. Chem.* **36**, 3804–3805 (1997).

ACKNOWLEDGMENTS

Funding: This work was primarily supported by the US Department of Energy (DOE), Office of Science, Basic Energy Sciences, Materials Sciences and Engineering Division. This material is based upon work supported by Laboratory Directed Research and Development (LDRD) funding from Argonne National Laboratory, provided by the Director, Office of Science, of the DOE under contract no. DE-AC02-06CH11357. EDX and SEM work was performed at the Center for Nanoscale Materials and Advanced Photon Source, both DOE Office of Science User Facilities, was supported by the DOE, Office of Basic Energy Sciences, under contract no. DE-AC02-06CH11357. Work at the Advanced Photon Source (APS) at Argonne National Laboratory was supported by the DOE, Office of Science, Office of Basic Energy Sciences under contract no. DE-AC02-06CH11357. Small-angle X-ray scattering works were performed at the DuPont-Northwestern-Dow Collaborative Access Team (DND-CAT) located at Sector 5 of the Advanced Photon Source (APS). DND-CAT is supported by Northwestern University, The Dow Chemical Company, and DuPont de Nemours, Inc. Z.W. acknowledges support from the Ford Motor Company, and C.W. acknowledges support from the DOE, Office of Science, Basic Energy Sciences under grant DE-SC0014520. Microscopy was conducted in the EPIC facility (RRID: SCR_026361) of Northwestern University's NUANCE Center, which has received support from the SHyNE Resource (NSF ECCS-2025633), the International Institute for Nanotechnology (IIN), and Northwestern's MRSEC program (NSF DMR-2308691). This work is based on research conducted at the Center for High-Energy X-ray Sciences (CHEXS), which is supported by the National Science Foundation (BIO, ENG, and MPS Directorates) under award DMR-2342336. **Author contributions:** The work was conceived by H.Z., X.Z., D.-Y.C., and M.G.K. with input from all authors. H.Z. carried out the synthesis, laboratory and synchrotron x-ray diffraction, electrical transport measurements, data analysis, and writing. X.Z. carried out data analysis and writing. Z.W. and C.W. performed first-principles electronic band structure calculations and data analysis. P.E.M. and V.P.D. carried out high-resolution transmission electron microscopy measurements and data analysis. Y.W. performed electrical transport measurements. D.T.K. and S.J.W. performed synchrotron small-angle x-ray scattering. S.H.L. carried out synchrotron powder x-ray diffraction. H.Z. and S.R. performed single-crystal synchrotron x-ray diffraction measurements. S.R., D.-Y.C., and M.G.K. supervised the project. **Competing interests:** The authors declare no competing financial interests. **Data and materials availability:** All data, including structural and physical property characterizations, and detailed structure descriptions are available in the manuscript or in the supplementary materials. Additional crystallographic information files (CIFs) are CSD nos. 2402260, 2402470, and 2473033 to 2473041.

SUPPLEMENTARY MATERIALS

science.org/doi/10.1126/science.aea8088
Materials and Methods; Supplementary Text; Figs. S1 to S31; Tables S1 to S3; References (*39*–*51*); Data S1

Submitted 21 July 2025; accepted 2 October 2025

10.1126/science.aea8088